The Cryosphere Discuss., 8, 2213–2241, 2014
www.the-cryosphere-discuss.net/8/2213/2014/
doi:10.5194/tcd-8-2213-2014

The Cryosphere
Discussions
Open Access

A sea ice concentration estimation algorithm utilizing radiometer and SAR data

J. Karvonen

Finnish Meteorological Institute (FMI), Helsinki, PB 503, 00101, Finland

Received: 7 March 2014 – Accepted: 17 April 2014 – Published: 28 April 2014

Correspondence to: J. Karvonen (juha.karvonen@fmi.fi)

Published by Copernicus Publications on behalf of the European Geosciences Union.

Abstract

We have studied the possibility of combining the high-resolution SAR segmentation and ice concentration estimated by radiometer brightness temperatures. Here we present an algorithm for mapping a radiometer-based concentration value for each SAR segment. The concentrations are estimated by a MLP neural network which has the AMSR-2 radiometer polarization ratios and gradient ratios of four radiometer channels as its inputs. The results have been compared numerically to the gridded FMI ice chart concentrations and high-resolution AMSR-2 ASI algorithm concentrations provided by University of Hamburg and also visually to the AMSR-2 bootstrap algorithm concentrations, which are given in much coarser resolution. The results when compared to FMI ice charts were very promising.

1 Introduction

Ice concentration is defined as the ratio of the ice covered area to the total area for a given sea region. From this definition directly follows that ice concentration is dependent on the resolution of the measurement. This fact also complicates direct comparison to different ice concentration products in different resolutions. Space-borne radiometers are an important data source capable of estimating the ice concentration in a resolution of around 10 km or even coarser. Also other space-borne instruments for estimating the ice concentration have been used. The advantage of radiometers, like AMSR-2 (Advanced Microwave Scanning Radiometer 2) is that they have a daily coverage over most of the ice-covered sea areas. Algorithms producing ice concentration from radiometer data are e.g. the NASA team algorithm (Cavalieri et al., 1984), the bootstrap algorithm (Comiso, 1986, 1995) used by the National Sea Ice Data Center (NSIDC), and the Artist Sea Ice (ASI) algorithm (Kaleschke et al., 2001; Spreen et al., 2008) of University of Bremen (UB). The ASI algorithm utilizing the full resolution of the AMSR-2 has been introduced and is operationally providing Arctic and

TCD
8, 2213–2241, 2014

Antarctic ice concentration at University of Hamburg (UH) (Beitsch et al., 2013; Beitsch and Kaleschke, 2014). Here we also provide a comparison of our results to these fine-resolution radiometer ice concentration estimates. Ice concentration in a finer resolution can also be retrieved from instruments capable of measuring surface temperature, but these instruments operate at (infrared) wavelengths not penetrating the cloud cover. Due to relatively long cloudy periods, which can last even several weeks, during the wintertime there can occur long temporal gaps in these measurements. One example of such algorithms is the MPA (MODIS potential open water algorithm) (Drüe and Heinemann, 2004), developed at University of Bonn, using the Moderate Resolution Imaging Spectroradiometer (MODIS) instrument data for ice concentration retrieval. Synthetic aperture radar (SAR) data, with high resolution, large spatial coverage and capability to acquire data through cloud cover, have not yet widely been used in measuring sea ice concentration. Some studies using single-band SAR for estimation of ice concentration have however been made, e.g. those reported in (Bovith and Andersen, 2005; Berg, 2011; Karvonen, 2012; Karvonen et al., 2012). Automated sea ice classification schemes, which implicitly include ice concentration or an open water class, based on single-band SAR texture have also been proposed, e.g. in (Clausi and Jernigan, 2000; Clausi, 2001; Deng and Clausi, 2004, 2005; Maillard et al., 2005; Yu and Clausi, 2007; Ochilov and Clausi, 2012; Leigh et al., 2014). These methods use multiple techniques, like the gray-level co-occurrence texture features (Haralick at al., 1973), Markov random fields (MRF) (Rue and Held, 2005), and Gabor filters (Pichler et al., 1996; Clausi and Jernigan, 2000) for classifying the sea ice SAR data. Dokken (Dokken et al., 2000) developed a SAR ice concentration algorithm which is a combination of mean ratio (relating average SAR backscatter to typical open water and sea ice values), a local threshold and a wavelet method (to detect edges around ice floes) for RADARSAT-1 and ERS SAR imagery. It has also been shown that using dual-polarized C-band SAR data (HH/HV) improves the ice concentration estimation compared to single-channel SAR (HH) (Karvonen, 2014). A method for ice classification into four ice classes and open water by combining SSM/I radiometer ice concentration and SAR data was introduced in (Kaleschke and Kern, 2000). Here we propose a novel method combining high-resolution SAR segmentation and the lower-resolution radiometer ice concentration estimation to yield ice concentration estimates with improved areal boundaries defined by the SAR resolution. The algorithm is based on SAR segmentation and on multi-layer perceptron (MLP) neural network.

2 Study area, time and data

We studied our novel algorithm over the Baltic Sea. The study area defined by the upper left and lower right corner was from (56.0° N, 16.0° E) to (66.0° N, 31.0° E). The areas is shown in Fig. 1. The period of the study was from 23 January 2014 to 11 February 2014. The radiometer data were AMSR-2 radiometer level 1R brightness temperature data Maeda (2013). The SAR data were dual-polarized (HH/HV polarization combination) RADARSAT-2 ScanSAR Wide mode data. In this study we only utilized the HH channel of the SAR data. The ice concentration estimates were produced in Mercator projection, mapped and re-sampled to the resolution of 500 m which corresponds to the resolution of our SAR mosaics. The data set was divided into training data set, consisting of SAR mosaics and AMSR-2 brightness temperature mosaics from 23 January 2014 to 1 February 2014, and test data set, consisting of SAR mosaics and the corresponding daily AMSR-2 brightness temperature mosaics from 2 February 2014 to 11 February 2014. Both data sets included 10 SAR mosaics and the corresponding daily AMSR-2 brightness temperature images.

3 Ice concentration estimation algorithm

3.1 SAR Processing

The SAR imagery were processed according to our standard procedure, first they were calibrated and rectified to Mercator projection, then an incidence angle correction was

TCD
8, 2213–2241, 2014

applied according to (Makynen et al., 2002). After this daily SAR mosaics were computed by remapping the SAR images into the study area such that newer data was always overlayed over older data, producing mosaics with the newest SAR data at each mosaic grid cell or pixel. The resolution of the SAR mosaics was 500 m. After this a segmentation step is performed for the daily mosaic. Here we have used a Markov Random Field (MRF) based segmentation adapted from (Kato et al., 1992; Berthod et al., 1996), but in practice any feasible segmentation, such as ICM (Iterated Conditional Modes) (Besag, 1986) or even K-means (MacQueen, 1967) can be used with rather similar results. The SAR segments with smaller size than 100 pixels (corresponding to an area of 25 km^2) were combined to the adjacent larger segments with the closest HH backscattering value (by an iterative process). The incidence angle correction has been designed for sea ice and in general it does not work over the open water areas, where the SAR backscattering is dependent on the water surface roughness i.e. waves. Wave conditions can change rapidly depending on the winds and a good incidence angle correction over open water would require reliable wave magnitude and direction information (i.e. 2-dimensional wave spectrum). Due to the varying wave conditions the backscattering from open water in different SAR images can vary significantly. This naturally can be seen in SAR mosaics and affects the SAR segmentation in these areas. However, this effect is not a problem in e.g. concentration estimation or segment classification as far as open water and segments with sea ice are separated by the segmentation.

3.2 AMSR-2 processing

The AMSR-2 brightness temperature data were processed into daily mosaics similarly to SAR mosaicking, i.e. mosaics such that the new data was always written over older data. This data was presented in 10 km resolution. The brightness temperatures used in this study were from the 18.7 GHz, 23.8 GHz, 36.5 GHz and 89.0 GHz, here denoted by 18 GHz, 23 GHz, 36 GHz and 89 GHz channels, respectively. All the AMSR-2 channels have both H and V polarizations. From the daily brightness temperature mosaic data all the polarization ratios (PR) and gradient ratios (GR) were derived according to the following equations:

$$\mathrm{PR}(f) = \frac{T_\mathrm{B}(f,V) - T_\mathrm{B}(f,H)}{T_\mathrm{B}(f,V) + T_\mathrm{B}(f,H)}, \tag{1}$$

and

$$\mathrm{GR}(f1,f2,p) = \frac{T_\mathrm{B}(f1,p) - T_\mathrm{B}(f2,p)}{T_\mathrm{B}(f1,p) + T_\mathrm{B}(f2,p)}. \tag{2}$$

By computing the polarization ratios for all the four frequencies, denoted by f, and the pairwise gradient ratios for all the four frequencies and for the two polarization, denoted by p, we get four polarization ratios and 12 gradient ratios at each grid cell. These are then used in the concentration estimation. The advantage of using polarization ratios is that they reduce the dependence on temperature, e.g. (Steffen et al., 1992). If the brightness temperatures were used, then also temperature estimates (e.g. from a numerical weather prediction model) or measurements at each grid point would be necessary for reliable ice concentration estimation.

A land mask, which was derived from the GSHHS coastline data Wessel and Smith (1996), was applied to the brightness temperatures in their original (low) resolution, after this the values were extrapolated to cover a larger area overlapping the land areas, This technique was used to avoid re-sampling artifacts in the next phase. After this the brightness temperature grids were up-sampled to the SAR mosaic resolution (500 m) and a land masking in this high resolution was applied. This approach enables us to compute ice concentration estimates for the coastal SAR segments also.

3.3 Combining brightness temperatures and SAR

After SAR segmentation we computed the mode of each polarization ratio and gradient ratio for each SAR segment. The mode was computed from up-sampled MODIS

TCD
8, 2213–2241, 2014

polarization ratio and gradient ratio grids. The concentration estimation for each SAR segment was based on these segment-wise modes of polarization and gradient ratios as MLP inputs. In this way we are able to produce an ice concentration estimate in the SAR mosaic resolution. The boundaries of different ice concentration areas are in the SAR resolution. Naturally the method is unable to extract smaller details than defined by the AMSR-2 resolution, but as concentration is a function of the resolution we still get reasonable concentration estimates over these areas also.

3.4 Concentration estimation

The ice concentration estimation is based on the Multi-Layer Perceptron (MLP) neural network. The neural network was trained using the error backpropagation algorithm (Haykin, 1999). The neural network was trained using the FMI gridded ice charts as its reference input. The hidden layer nonlinearities were implemented using the hyperbolic tangent (tanh) function. The single unit or artificial neuron of the output layer corresponding to the one MLP output (the estimated ice concentration) was linear. Feed-forward neural networks, such as MLP, with a single hidden layer of sigmoidal units are capable of approximating any continuous multivariate function, to any desired degree of accuracy (Hornik, 1989).

The output y_i of each MLP unit with index i is computed as

$$y_i = f_i\left(\sum_j W_{ij} y_j\right), \tag{3}$$

where f_i is the activation function of the unit (also known as a node or a neuron) i. At the hidden layer the mapping is $f_i(x) = \tanh(x)$, and at the output layer the mapping is linear, i.e. $f_o(x) = x$. The weights W_{ij} are related to each input y_j, which are also outputs from the previous MLP layer (or inputs at the input layer). In the training phase the outputs are first computed in the forward direction and then the error is propagated back from the MLP output layer, i.e. starting from the error between the ice concentration estimate given by the MLP and the desired ice concentration defined by the training data, towards the input layer. A detailed derivation and presentation of the error backpropagation learning rule can be found e.g. in Haykin (1999). In our case the only output is the ice concentration, and thus our MLP has only one output unit. In the training phase the weights W_{ij} are updated towards the negative gradient of the error function at each node. To include a constant term (W_{k0}) also 1.0 is input into each MLP unit.

The used MLP architecture was 17-20-1, i.e. sixteen inputs corresponding to the four polarization ratios, 12 gradient ratios and the constant term (input 1.0), 20 hidden layer nonlinear units and one linear output layer unit, whose output is the ice concentration estimate. A schematic diagram of the MLP used is shown in Fig. 2. The number of the hidden layer units was determined experimentally. Because the algorithm makes the estimation segment-wise, not pixel-wise, the estimation is rather fast, and we just selected the number of hidden-layer neurons to be large enough to get good estimates.

We used the so-called epoch training, i.e. the whole training data set is iteratively fed through the MLP in a random order, and each iteration corresponds to one epoch. In the following equations the epochs are indicated by the time variable t, which is an integer number starting from one. The learning rate parameter μ is adaptive. At the first epoch the learning rate is set to 0.005 and it is adjusted after each epoch t depending on the total MLP error E:

$$\mu(t+1) = 1.05\mu(t), \quad \text{if } E(t) < E(t-1), \tag{4}$$

$$\mu(t+1) = 0.70\mu(t), \quad \text{if } E(t) \geq E(t-1). \tag{5}$$

The number of training epochs used was 20 000. The MLP coefficients W_{ij} were initialized randomly, and the MLP coefficients corresponding to the minimum MLP total error E among 40 training runs were selected as the final MLP parameters, which are then used in the ice concentration estimation. This approach guarantees exclusion of a poor selection of the initial MLP weight coefficient configuration.

Discussion Paper | Discussion Paper | Discussion Paper | Discussion Paper |

TCD

8, 2213–2241, 2014

A sea ice concentration estimation algorithm

J. Karvonen

4 Evaluation

We evaluated the algorithm results by comparing them to the FMI digitized ice chart grids, which have a nominal resolution of 1 km, and to the high-resolution (3.125 km) UH ASI AMSR-2 algorithm (Beitsch et al., 2013; Beitsch and Kaleschke, 2014) results. We also made a visual comparison to the results of the AMSR-2 bootsrap algorithm ice concentrations provided by JAXA (Maeda, 2013; JAXA, 2013).

We also performed some comparisons over an Arctic Sea test area (Kara and Barents Seas), over which we make SAR mosaics daily. We used the same training data as used for the Baltic Sea, and the comparison to the AMSR-2 level 2 concentration results showed good agreement. An example of the Kara and Barents sea area ice concentration estimates based on the AMSR-2 bootstrap algorithm and our algorithm is shown in Fig. 5.

Comparison between SAR based ice concentration and reference data were made by using three error measures, L_1 error E_{L1}, the signed L_1 error E_{sgn} (describing the bias), and root mean square (RMS) error E_{RMS}:

$$E_{L1} = \frac{1}{N_s} \sum_{i=1}^{N_s} \left| C_i^{\mathrm{est}} - C_i^{\mathrm{ref}} \right|, \tag{6}$$

$$E_{\mathrm{sgn}} = \frac{1}{N_s} \sum_{i=1}^{N_s} \left(C_i^{\mathrm{est}} - C_i^{\mathrm{ref}} \right). \tag{7}$$

$$E_{\mathrm{RMS}} = \sqrt{\frac{1}{N_s} \sum_{i=1}^{N_s} \left(C_i^{\mathrm{est}} - C_i^{\mathrm{ref}} \right)^2} \tag{8}$$

N_s is the number of pixels or grid cells computed over the whole ice concentration estimate grid area, C_i^{est} is the estimated concentration, and C_i^{ref} is the reference concentration at each pixel indicated by the index i. The error measures were computed

TCD
8, 2213–2241, 2014

over the SAR image mosaic area (with the grid cell spacing of 500 m), and the reference data were sampled into the same resolution by using bi-linear sampling. The comparisons were also grid cell based comparisons in the SAR mosaic resolution of 500 m. $E_{L1}(\geq 0)$ describes the mean absolute error, and E_{sgn} describes the bias or systematic error. If $E_{\text{sgn}} < 0$, the algorithm underestimates, and if $E_{\text{sgn}} > 0$, the algorithm overestimates the ice concentration compared to the reference data. RMS error represents the sample standard deviation of the differences between the estimated values and the reference values.

The comparison results can be seen in Table 1, the errors are given in percentage points. We also provide the standard deviations for the error measures, describing the variations between the images. For the training data set the ice concentration is slightly overestimated (2.95 percentage points) and for the test data set slightly underestimated (3.91 percentage points), the mean L_1 error for the training and test data sets is practically the same, about 8.7 percentage points. The standard deviations of the errors are relatively low for all the error measures indicating that the errors are quite similar for all the data. Two examples of the estimation result, the corresponding FMI ice chart concentrations, and the corresponding bootstrap algorithm concentration estimates can be seen in Figs. 3 and 5. In the SAR mosaic and segmentation result (see Fig. 3) we can see that the open water areas produce different backscattering depending on the prevailing wave conditions and this can be seen as clear SAR frame boundaries in the image mosaic and as separate segments in the segmentation result. However, in the ice covered areas the SAR frame boundaries are not visible indicating that the incidence angle correction for sea ice has been successful. In these figures we can for example see that the new algorithm is unable to capture parts of the ice-covered areas in the northern parts of Gulf of Finland. These areas are near the coast and problematic for radiometer. However, the estimates for the ice zones in the Gulf of Riga (southeastern part of the images) corresponds the ice chart concentration much better than the bootstrap algorithm result in both cases. Also in Fig. 5, the ice concentration of the ice areas in the mid-parts of the Gulf of Bothnia (in the north in the images) give higher concentrations better comparable to the ice chart concentrations, the bootstrap algorithm seems to underestimate the concentration in these areas.

In Figs. 4 and 6 we show the differences between the FMI ice chart and our algorithm result, and also a similar comparison to the UH ASI algorithm results. The ASI concentration estimates are also included in Figs. 3 and 5. This version utilizes the full resolution AMSR-2 data, and it can even capture the ice-covered zone in the northern Gulf of Finland. However, in the coastal zone it seems to overestimate the ice concentration. The largest differences between the FMI ice chart concentration and ASI concentration occur at the ice boundaries (ice edge), which have higher precision in FMI ice charts and also in our combined radiometer/SAR product. The numerical results of this comparison are given in Tables 2 and 3. In some open water areas in the western parts of the Arctic test area mosaic there occur some overestimations of the ice concentration. These are probably due to different weather conditions and open water signatures than in the Baltic Sea (training data set), and would also probably be corrected by including also data from the Arctic in the training phase.

The comparisons to the bootstrap ice concentrations provide by JAXA were visual evaluations of the differences. The results of our algorithm correspond to the results of the bootstrap algorithm quite well. However, our algorithm also gives ice estimates over the coastal areas, and at the boundaries of different ice concentration zones are in the SAR mosaic resolution. The results of our algorithm and bootstrap ice concentrations are also seen in Figs. 3 and 5. We did not make numerical comparisons, because of the significantly different resolutions, in this case the effect of the resolution would probably had contributed more to the computed error than the actual error. Some rough estimates of the effect of the different resolutions to the concentration estimation error can be found e.g. in (Karvonen, 2014).

We also made a visual comparison for two ice concentration estimations over an Arctic ocean test area in the Barents and Kara Seas. Also in these areas the bootstrap algorithm concentrations and concentrations produced by our algorithm were in good agreement, as an example see Fig. 7, even though the training was performed with a rather limited set of Baltic Sea data. We also compared our algorithm results to the ASI high-resolution results over this area for our two test images, the resulting difference map for the case shown in Fig. 7 is shown in Fig. 8. For this comparison we also give the numerical errors in Table 2, but because we only used two Arctic scenes (daily mosaics) and the errors for both of them were rather similar, we do not provide the standard deviations.

5 Conclusion and discussion

The comparison results to FMI ice charts were better than for example those reported for dual-polarized SAR data in (Karvonen, 2014). The best concentration estimates can very likely be achieved by combining SAR data and using radiometer data as a background value, such as in (Karvonen et al., 2008) for ice thickness, and refining the segment-wise ice concentrations, given by the algorithm presented here, based on the high resolution SAR data.

The training was performed using the polarization ratios and gradient ratios, because they provide a more stable basis for the ice concentration estimation with respect to the temperature changes. We also studied estimation by directly feeding the brightness temperatures into the MLP, but the MLP convergence was slower and estimation results worse with this approach. The reason for this behavior was obviously that to be able to also model the temperature dependence a representative training data set describing a wide range of temperature conditions would be required, and our training data set of ten day mosaics was too small for that purpose. However, it seems to be large enough when using ratios instead of brightness temperatures directly. We believe even better results can be achieved by using an extensive representative training data set covering all possible ice types and weather conditions. However, already this experiment clearly indicates the potential of the methodology for providing high-resolution operational ice concentration estimates.

We have used the re-sampled AMSR-2 L1R data having a resolution of about 10 km. We can see that the ASI algorithm utilizing the full AMSR-2 resolution (full resolution of the higher frequency channels) is capable of distinguishing details which are not all visible in the L1R data. It would be desirable to use the best possible resolution in the future operational algorithm and we are going to adapt our MLP algorithm to work with the high-precision data also, and after this high-resolution radiometer estimate we can still refine the segment boundaries based on SAR data to yield improved precision. Actually, all we need to do is to train the algorithm with suitably sampled high-resolution data for a representative training data set, after this it is capable of utilizing the full resolution.

The comparison results show that our algorithm estimates are closer to the FMI ice charts than the other two reference algorithms (bootstrap and ASI). This was an expected result, because the FMI ice charts are mainly based on visual interpretation of SAR data, and FMI ice charts and SAR data has been used in the training, and thus our algorithm has in a way been adapted to the FMI ice charts.

We were also surprised of the good estimation results in the Arctic test area, because the training data was from a relatively short period and from the Baltic Sea area. This can at least partly be explained by the fact that the in our Arctic test area there mainly exist only seasonal sea ice, only a little multi-year can appear in the northern parts of the area. In areas with more multi-year ice the algorithm should be trained with similar data for reliable ice concentration estimates. Because in the Arctic we do not have digitized ice charts in our use, we should use other data sources for the training. One such data source could be results of other radiometer ice concentration algorithms, like the bootstrap and ASI algorithms used as reference data here, refined by SAR imagery as presented in Sect. 3.3.

The advantage of the MLP approach is that it is not necessary to define parameters related to the brightness temperatures or ratios, all we need is a representative training data set to train the MLP. The disadvantage is that the actual nonlinear mapping from the input parameters to ice concentration remains unknown. The mapping is naturally described by the MLP weights and MLP structure, but the physical relationship between inputs and outputs remains unclear.

The novel method results to improved accuracy of the boundaries of the ice zones. As it can be seen the largest differences between our algorithm results and the reference products typically appear at the boundaries of the segments corresponding to the ice edge. This indicates that our algorithm is capable of representing the boundaries of regions with different concentration in a resolution defined by the SAR mosaic resolution. There still are some differences when comparing to ice chart concentrations, especially in the coastal zones. This can be explained by the low resolution of the radiometer data: in the case of a narrow ice zone near the coast the ice concentration is not estimated correctly. Also there seem to be some low-concentration areas produced by our algorithm in areas where the ice charts indicate much higher concentrations. It is very difficult to say whether these segments are due to the more precise distinguishing capability of the algorithm (when the ice analyst has given a concentration value for a larger polygon), or an estimation error (e.g. due to wet snow or water over the ice). In any case the use of segment-wise brightness temperature value modes seems to improve the ice concentration estimation significantly compared to radiometer data alone with respect to the gridded ice chart concentrations. It can be expected that applying our algorithm to radiometer data in a higher resolution the results would be even better, then the concentration of smaller ice areas and concentration areas near coasts would be estimated better.

References

Beitsch, A. and Kaleschke, L.: The February 2013 Arctic Sea Ice Fracture in the Beaufort Sea – a case study for two different AMSR2 sea ice concentration algorithms, Remote Sensing, accepted, 2014. 2215, 2221

Beitsch, A., Kaleschke, L., and Kern, S.: AMSR2 ASI 3.125 km Sea Ice Concentration Data, V0.1, Institute of Oceanography, University of Hamburg, Germany, digital media (ftp://ftp-projects.zmaw.de/seaice/ (last access: 28 April 2014)),, 2013. 2215, 2221

TCD

8, 2213–2241, 2014

A sea ice concentration estimation algorithm

J. Karvonen

Berg, A.: Spaceborne SAR in Sea Ice Monitoring: Algorithm Development and Validation for the Baltic Sea, Licentiate thesis, Technical Report 47L, Chalmers University of Technology, Gothenburg, Sweden, 2011. 2215
Berthod, M., Kato, Z., Yu, S., and Zerubia, J.: Bayesian image classification using Markov Random Fields, Image Vision Comput., 14, 285–295, 1996. 2217
Besag, J.: On the statistical analysis of dirty pictures, J. Roy. Stat. Soc. B, 48, 259–302, 1986. 2217
Bovith, T. and Andersen, S.: Sea Ice Concentration from Single-Polarized SAR data using Second-Order Grey Level Statistics and Learning Vector Quantization, Scientific Report 05-04, Danish Meteorological Institute, Copenhagen, Denmark, 2005. 2215
Cavalieri, D. J., Gloersen, P., and Campbell, W. J.: Determination of sea ice parameters with the NIMBUS 7 SMMR, J. Geophys. Res., 89, 5355–5369, 1984. 2214
Clausi, D. A.: Comparison and fusion of co-occurrence, Gabor, and MRF texture features for classification of SAR sea ice imagery, Atmosphere and Oceans, 39, 183–194, 2001. 2215
Clausi, D. A. and Jernigan, M. E.: Designing Gabor filters for optimal texture separability, Pattern Recogn., 33, 1835–1849, 2000. 2215
Comiso, J. C.: Characteristics of Arctic winter sea ice from satellite multispectral microwave observations, J. Geophys. Res., 91, 975–994, 1986. 2214
Comiso, J. C.: SSM/I Sea Ice Concentrations Using the Bootstrap Algorithm, NASA Reference Publication / Goddard Space Flight Center 1380, Greenbelt, Maryland, USA., 1995. 2214
Deng, H. and Clausi, D. A.: Gaussian MRF rotation-invariant features for image classification, IEEE T. Pattern Anal., 26, 951–955, 2004. 2215
Deng, H. and Clausi, D. A.: Unsupervised segmentation of synthetic aperture radar sea ice imagery using a novel Markov random field model, IEEE T. Geosci. Remote, 43, 528–538, 2005. 2215
Dokken, S. T., Hakansson, B., and Askne, J.: Inter-comparison of Arctic Sea ice concentration using RADARSAT, ERS, SSM/I and in-situ data, Can. J. Remote Sens., 26, 521–536, 2000. 2215
Drüe, C. and Heinemann, G.: High-resolution maps of the sea-ice concentration from MODIS satellite data, Geophys. Res. Lett., 31, L20403, doi:10.1029/2004GL020808, 2004. 2215
Geldsetzer, T. and Yackel, J. J.: Sea ice type and open water discrimination using dual co-polarized C-band SAR, Can. J. Remote Sens., 35, 73–84, 2009.

Haralick, R. M., Shanmugam, K., and Dinstein, I.: Textural features for image classification, IEEE T. Syst. Man Cyb., SMC-3, 610–621, 1973. 2215

Haykin, S. S.: Neural Networks, a Comprehensive Foundation, 2nd edn., Prentice Hall, Upper Saddle River, N.J., USA., 183–196, 1999. 2219, 2220

Hornik, K., Stinchcombe, M., and White, H.: Multilayer feedforward networks are universal approximators, Neural Networks, 2, 359–366, 1989. 2219

JAXA: Descriptions of GCOM-W1 AMSR2 Level 1R and Level 2 Algorithms, Rev.A, available at: http://suzaku.eorc.jaxa.jp/GCOM_W/data/data_w_algorithm.html (last access: 28 April 2014), 2013. 2221

Kaleschke, L. and Kern, S.: ERS-2 SAR Image Analysis for Sea Ice Classification in the Marginal Ice Zone, Proc. IEEE International geoscience and remote sensing symposium 2000 (IGARSS 2000), V, 3038–3040, July 24-28, 2000, Honolulu, Hawaii, USA., 2000. 2216

Kaleschke, L., Lupkes, C., Vihma, T., Haarpaintner, J., Bochert, A., Hartmann, J., and Heygster, G.: SSM/I sea ice remote sensing for mesoscale ocean-atmosphere interaction analysis, Can. J. Remote Sens., 27, 526–537, 2001. 2214

Karvonen, J.: Baltic Sea ice concentration estimation based on C-Band HH-Polarized SAR data, IEEE J. Sel. Top. Appl., 5, 1874–1884, doi:10.1109/JSTARS.2012.2209199, 2012. 2215

Karvonen, J.: Baltic Sea ice concentration estimation based on C-Band Dual-Polarized SAR data, IEEE T. Geosci. Remote, doi:10.1109/TGRS.2013.2290331, to be published, 2014. 2215, 2223, 2224

Karvonen, J., Simila, M., and Makynen, M.: Open water detection from Baltic Sea Ice Radarsat-1 SAR imagery, IEEE Geosci. Remote S, 2, 275–279, 2005.

Karvonen, J., Cheng, B., and Simila, M.: Ice Thickness Charts Produced by C-Band SAR Imagery and HIGHTSI Thermodynamic Ice Model, Proc. of the Sixth Workshop on Baltic Sea Ice Climate, 71–81, 25–28 August 2008, Lammi, Finland 2008. 2224

Karvonen, J., Cheng, B., Vihma, T., Arkett, M., and Carrieres, T.: A method for sea ice thickness and concentration analysis based on SAR data and a thermodynamic model, The Cryosphere, 6, 1507–1526, doi:10.5194/tc-6-1507-2012, 2012. 2215

Kato, Z., Zerubia, J., and Berthod, M.: Satellite Image Classification Using a Modified Metropolis Dynamics, in: Proceedings of IEEE International Conference on Acoustics, Speech and Signal Processing (ICASSP 92), 3, 23–26 March 1992, San Francisco, California, USA, 573–576, March, 1992. 2217

Kern, S.: A new algorithm to retrieve the sea ice concentration using weather-corrected 85 GHz SSM/I measurements, Ph.D. thesis, Dept. Physics Elect. Eng., Univ. Bremen, Bremen, Germany, 2001.

Kern, S. and Heygster, G.: Sea-ice concentration retrieval in the antarctic based on the SSM/I 85.5 GHz polarization, Ann. Glaciol., 33, 109–114, 2001.

Kern, S., Kaleschke, L., and Clausi, D. A.: A comparison of two 85-GHz SSM/I ice concentration algorithms with AVHRR and ERS-2 SAR imagery, IEEE T. Geosci. Remote, 41, 2294–2306, 2002.

Leigh, S., Wang, Z., and Clausi, D. A.: Automated ice-water classification using dual polarization SAR satellite imagery, IEEE T. Geosci. Remote, 52, 5529–5539, 2014. 2215

MacQueen, J. B.: Some Methods for classification and Analysis of Multivariate Observations, in: Proceedings of 5th Berkeley Symposium on Mathematical Statistics and Probability, 21 June 21–18 July 1965 and 27 December 1965–7 June 1966, University of California Press., 281–297, 1967. 2217

Maeda, T.: AMSR2 L1R Product, JAXA, available at: http://suzaku.eorc.jaxa.jp/GCOM_W/materials/product/AMSR2_L1R.pdf (last access: 28 April 2014), 2013. 2216, 2221

Maillard, P., Clausi, D. A., and Deng, H.: Map-guided sea ice segmentation and classification using SAR imagery and a MRF segmentation scheme, IEEE T. Geosci. Remote, 43, 2940–2951, 2005. 2215

Makynen, M., Manninen, T., Simila, M., Karvonen, J., and Hallikainen, M.: Incidence angle dependence of the statistical properties of the C-Band HH-Polarization backscattering signatures of the Baltic Sea Ice, IEEE T. Geosci. Remote, 40, 2593–2605, 2002. 2217

Ochilov, S. and Clausi, D. A.: Operational SAR sea-ice classification, IEEE T. Geosci. Remote, 50, 4397–4408, 2012. 2215

Pichler, O., Teuner, A. S., and Hosticka, B. J.: A comparison of texture feature extraction using adaptive gabor filtering, pyramidal and tree structured wavelet transforms, Pattern Recogn., 29, 733–742, 1996. 2215

Rue, H. and Held, L.: Gaussian Markov Random Fields: Theory and Applications, CRC Press, 2005. 2215

Spreen, G., Kaleschke, L., and Heygster, G.: Sea ice remote sensing using AMSR-E 89-GHz channels, J. Geophys. Res., 113, C02S03, doi:10.1029/2005JC003384, 2008. 2214

Steffen, K., Key, J., Cavalieri, D. J., Comiso, J., Gloersen, P., St. Germain, K., and Rubinstein, I.: The estimation of geophysical parameters using passive microwave algorithms, Ch. 10, in:

Discussion Paper | Discussion Paper | Discussion Paper | Discussion Paper |

Microwave Remote Sensing of Sea Ice, edited by: Carsey, F. D., American Geophysical Society/Wiley, Washington D.C., USA., 201–231, 1992. 2218
Yu, Q. and Clausi, D. A.: SAR sea-ice image analysis based on iterative region growing using semantics, IEEE T. Geosci. Remote, 45, 3919–3931, 2007. 2215
Wessel, P. and Smith, W. H. F.: A global self-consistent, hierarchical, high-resolution shoreline database, J. Geophys. Res., 101, 8741–8743, 1996. 2218

TCD
8, 2213–2241, 2014

Table 1. Errors compared to FMI ice charts for the training and test data sets, for both the data sets the number of scenes $N = 10$.

Measure	Signed error	L1 error	RMSE
Training data set			
Error	2.95	8.67	19.98
Std. dev.	3.33	2.02	2.42
Test data set			
Error	−3.91	8.66	21.28
Std. dev.	2.67	1.98	3.29

TCD
8, 2213–2241, 2014

A sea ice concentration estimation algorithm

J. Karvonen

Table 2. Errors compared to ASI ice concentrations for the test data set, and for two Arctic ocean cases (corresponding to two daily SAR mosaics).

Measure	Signed error	L1 error	RMSE
Test data set (Baltic)			
Error	−1.23	11.15	25.19
Std. dev.	7.8381	4.1529	5.3505
Arctic ocean test cases			
Error	−3.29	6.68	16.85

TCD
8, 2213–2241, 2014

TCD
8, 2213–2241, 2014

Table 3. Errors for the comparison between FMI ice charts and the ASI results.

Measure	Signed error	L1 error	RMSE
Test data set (Baltic)			
Error	5.38	11.81	27.30
Std. dev.	4.31	2.54	3.28

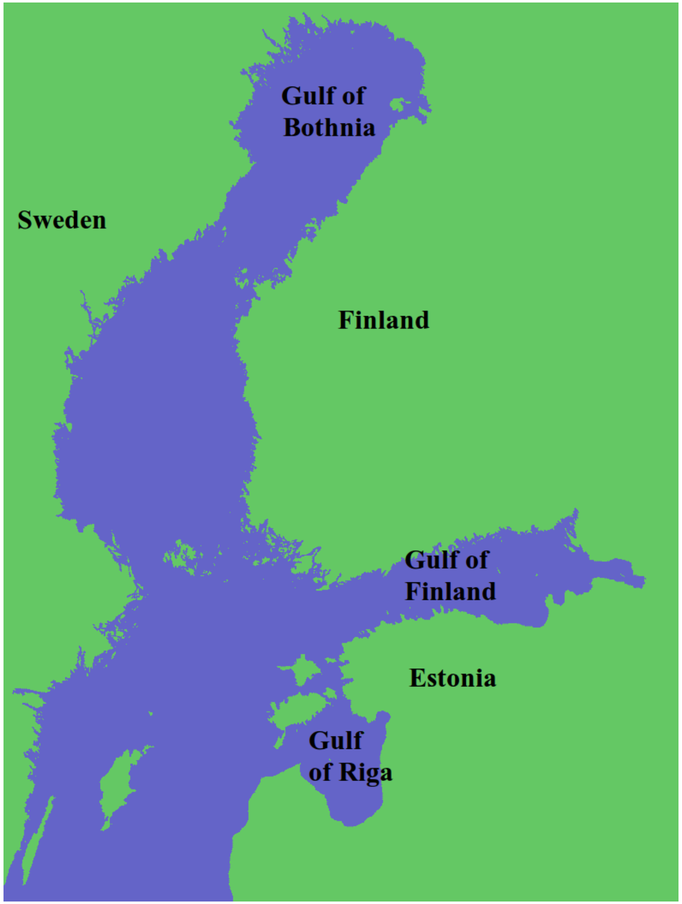

Fig. 1. The Baltic Sea study area.

TCD
8, 2213–2241, 2014

A sea ice concentration estimation algorithm

J. Karvonen

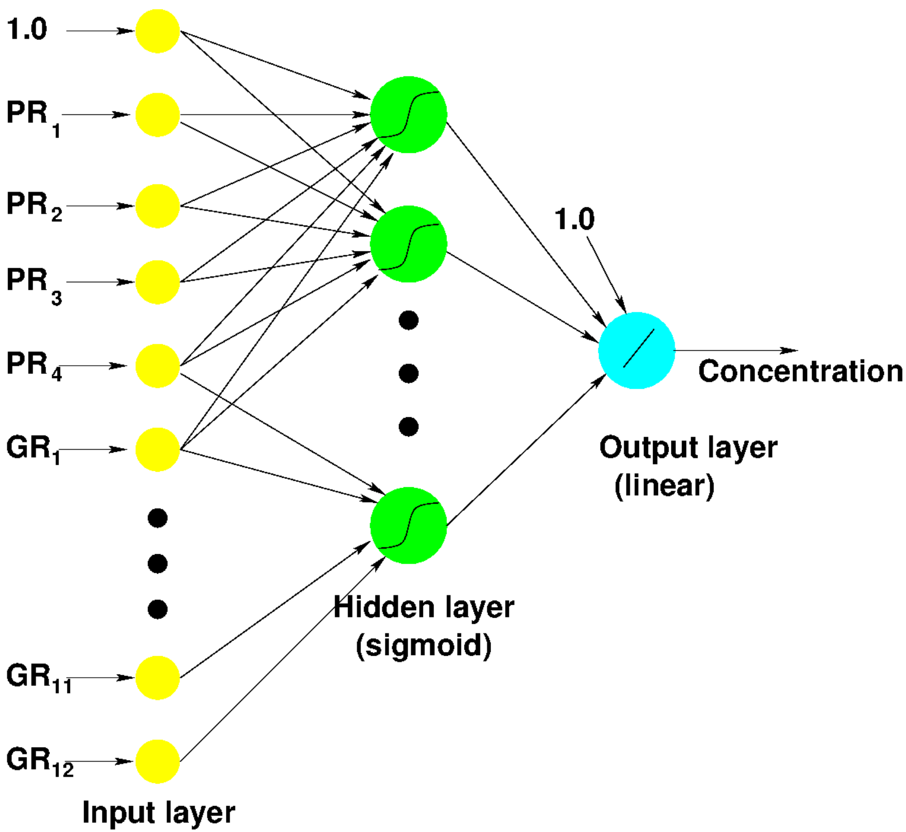

Fig. 2. A schematic diagram of the MLP architecture used, there are 17 input layer units (including the constant term 1.0), 20 hidden layer sigmoid units, and one linear output layer unit. For clarity not all the connection have been drawn in the figure.

TCD
8, 2213–2241, 2014

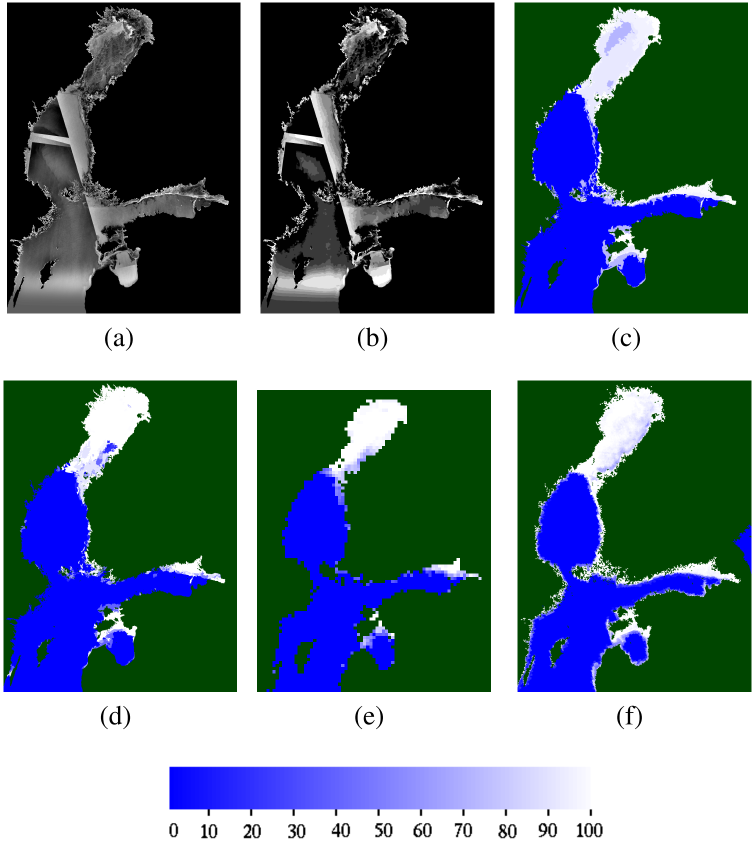

Fig. 3. SAR image mosaic of 2 February 2014, ©MDA **(a)**, segmentation result **(b)**, FMI ice chart grid ice concentration **(c)**, ice concentration estimate using our algorithm **(d)**, AMSR-2 bootstrap algorithm ice concentration **(e)**, ASI ice concentration **(f)**.

TCD
8, 2213–2241, 2014

A sea ice concentration estimation algorithm

J. Karvonen

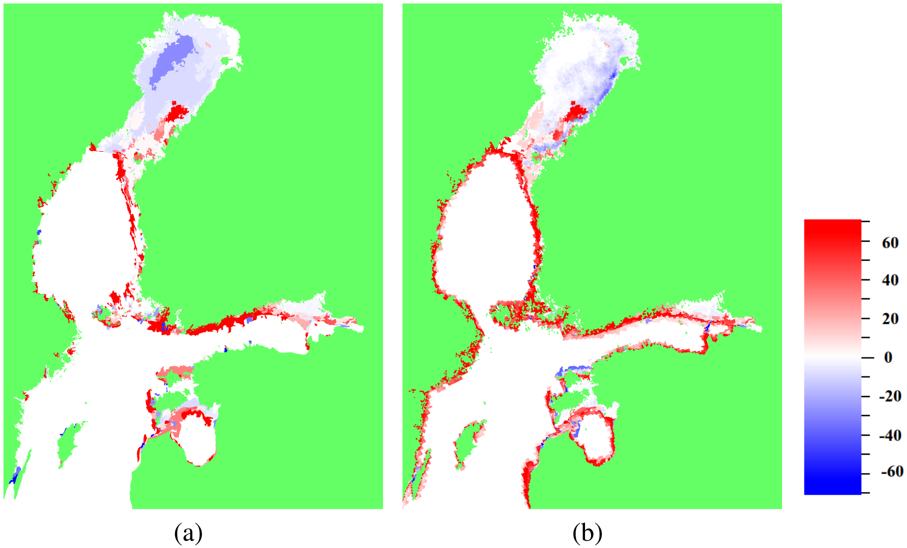

Fig. 4. Difference between the algorithm result and FMI ice chart concentration for 2 February 2014 **(a)**, and between the algorithm result and ASI concentration **(b)**. Overestimation produced by our algorithm with respect to the reference data is indicated by the blue tones (negative difference values) and underestimation by red (positive values).

TCD
8, 2213–2241, 2014

Title Page
Abstract | Introduction
Conclusions | References
Tables | Figures
Back | Close
Full Screen / Esc
Printer-friendly Version
Interactive Discussion

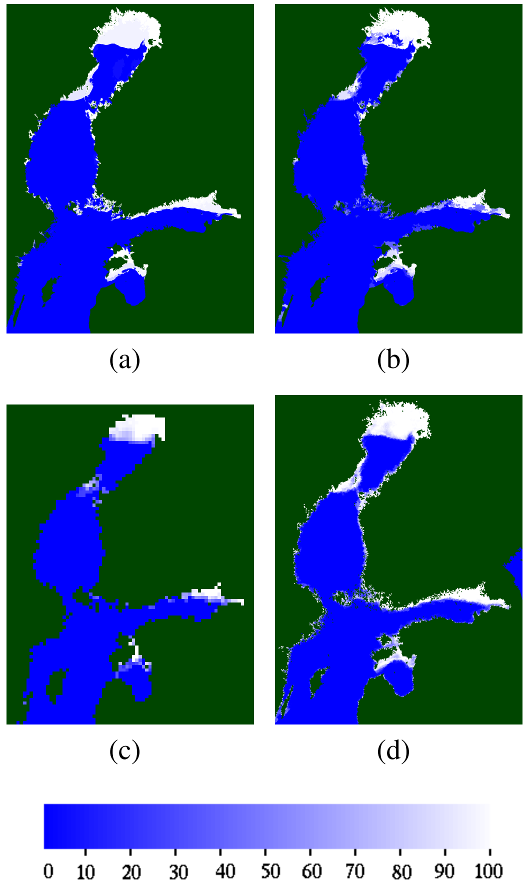

Fig. 5. FMI ice chart concentration grid for 11 February 2014 **(a)**, ice concentration estimate using our algorithm **(b)**, AMSR-2 bootstrap algorithm ice concentration **(c)**, and ASI ice concentration.

TCD
8, 2213–2241, 2014

A sea ice concentration estimation algorithm

J. Karvonen

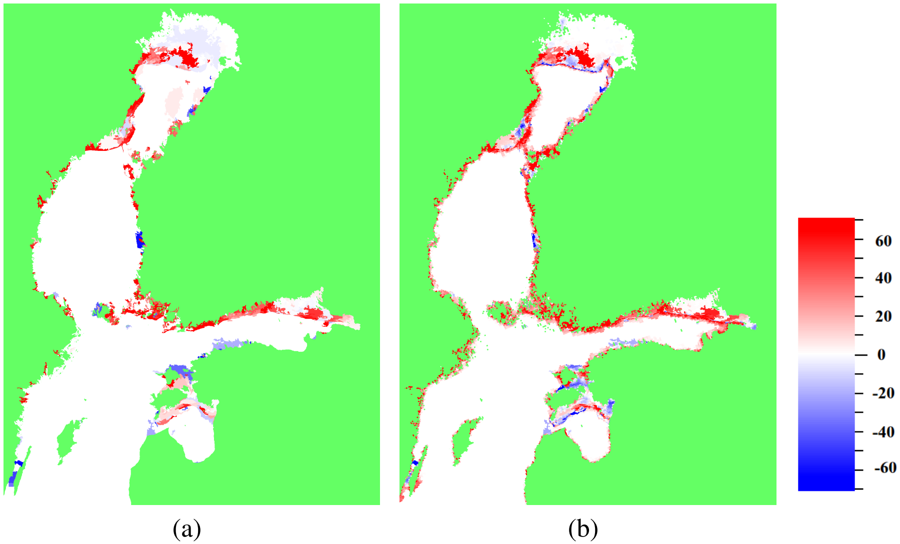

Fig. 6. Difference between our algorithm result and FMI ice chart concentration for 11 February 2014 **(a)**, and between the our result and ASI concentration **(b)**. Overestimation produced by our algorithm with respect to the reference data is indicated by the blue tones (negative difference values) and underestimation by red (positive values).

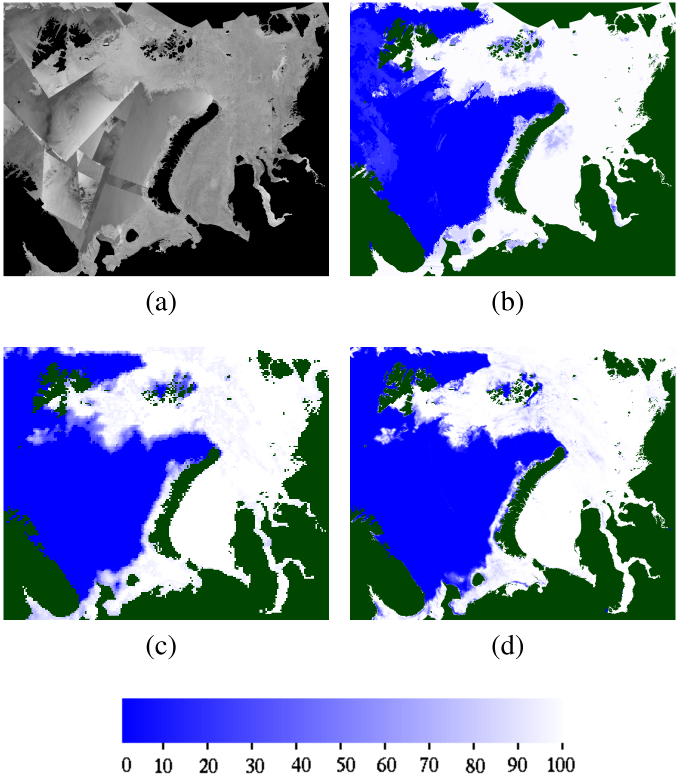

Fig. 7. An example of the Arctic ocean ice concentration estimation, the SAR mosaic of 2 February 2014 **(a)**, ice concentration estimate based on our algorithm **(b)**, the AMSR-2 level 2 ice concentration product **(c)**, and ASI ice concentration product **(d)**. Some parts of the area are not covered by the SAR mosaic and the concentration of our product is only given in the area of the SAR mosaic cover.

TCD
8, 2213–2241, 2014

A sea ice concentration estimation algorithm

J. Karvonen

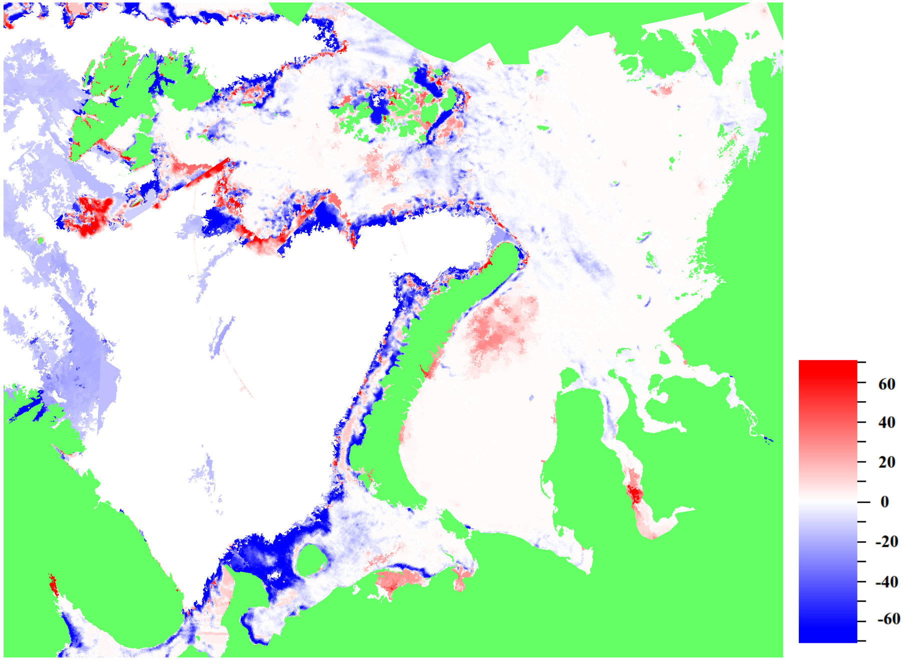

Fig. 8. The difference between the FMI algorithm concentration and ASI ice concentration for the Arctic study area, 2 February 2014. The values in the areas where our algorithm indicates higher concentration than ASI appear as blue and areas where our algorithm indicates lower concentration appear as red.

TCD
8, 2213–2241, 2014